Video Article

Fabrication and Characterization of Optical Tissue Phantoms Containing Macrostructure

Madeleine S. Durkee[1], Landon D. Nash[1], Fatemeh Nooshabadi[1], Jeffrey D. Cirillo[2], Duncan J. Maitland[1], Kristen C. Maitland[1]

[1]Department of Biomedical Engineering, Texas A&M University

[2]Deparment of Molecular Pathogenesis and Immunology, Texas A&M College of Medicine

Correspondence to: Kristen C. Maitland at kmaitland@tamu.edu

URL: https://www.jove.com/video/57031
DOI: doi:10.3791/57031

Keywords: Bioengineering, Issue 132, Tissue simulating phantoms, optical imaging, calibration standard, quality assurance, computer model validation, 3D printing

Date Published: 2/12/2018

Citation: Durkee, M.S., Nash, L.D., Nooshabadi, F., Cirillo, J.D., Maitland, D.J., Maitland, K.C. Fabrication and Characterization of Optical Tissue Phantoms Containing Macrostructure. *J. Vis. Exp.* (132), e57031, doi:10.3791/57031 (2018).

Abstract

The rapid development of new optical imaging techniques is dependent on the availability of low-cost, customizable, and easily reproducible standards. By replicating the imaging environment, costly animal experiments to validate a technique may be circumvented. Predicting and optimizing the performance of *in vivo* and *ex vivo* imaging techniques requires testing on samples that are optically similar to tissues of interest. Tissue-mimicking optical phantoms provide a standard for evaluation, characterization, or calibration of an optical system. Homogenous polymer optical tissue phantoms are widely used to mimic the optical properties of a specific tissue type within a narrow spectral range. Layered tissues, such as the epidermis and dermis, can be mimicked by simply stacking these homogenous slab phantoms. However, many *in vivo* imaging techniques are applied to more spatially complex tissue where three dimensional structures, such as blood vessels, airways, or tissue defects, can affect the performance of the imaging system.

This protocol describes the fabrication of a tissue-mimicking phantom that incorporates three-dimensional structural complexity using material with optical properties of tissue. Look-up tables provide India ink and titanium dioxide recipes for optical absorption and scattering targets. Methods to characterize and tune the material optical properties are described. The phantom fabrication detailed in this article has an internal branching mock airway void; however, the technique can be broadly applied to other tissue or organ structures.

Video Link

The video component of this article can be found at https://www.jove.com/video/57031/

Introduction

Tissue phantoms are used widely for system characterization and calibration of optical imaging and spectroscopy instruments, including multimodality systems incorporating ultrasound or nuclear modalities[1,2,3,4]. Phantoms provide a controlled optical environment for system characterization and quality control of multiple biological imaging techniques. Tissue-mimicking phantoms are useful tools in predicting system performance and optimizing system design for the physiological task at hand; for example, to predict the probing depth of spectroscopic probes for assessing tumor margins[5]. Optical properties and structural design of the phantoms can be tuned to mimic the specific physiological environment in which the instrument will be used, therefore allowing for both feasibility studies and verification of system performance[3,6,7]. Verification of imaging system performance with realistic optical phantoms prior to entering pre-clinical or clinical trials reduces the risk of malfunction or acquisition of unusable data during *in vivo* studies. The reproducibility and stability of optical phantoms make them customizable calibration standards for optical techniques to monitor intra- and inter-instrument variability, particularly in multicenter clinical trials with different instruments, operators, and environmental conditions[8,9].

Tissue-mimicking phantoms also serve as tunable and reproducible physical models for validation of theoretical optical models. Simulations aid in the design and optimization of *in vivo* optical instruments, while reducing the need for animal experiments[10,11]. The development and validation of optical simulations to accurately represent the *in vivo* environment can be encumbered by the complexity of the tissue structure, the biochemical content, and the location of the target or tissue within the body. Variability between subjects makes validation of theoretical models challenging using animal or human measurements. Polymer optical tissue phantoms allow for validation of theoretical models by supplying a known and reproducible optical environment in which to study photon migration[12,13,14,15].

For the purpose of system calibration, solid optical phantoms may consist of a single homogeneous slab of cured polymer with the optical scattering, absorption, or fluorescence tuned for the wavelengths of interest. Layered polymer phantoms are frequently used to mimic the depth variance of the tissue optical properties in epithelial tissue models[16,17]. These phantom structures are sufficient for epithelial imaging and modeling, because the tissue structure is fairly homogeneous through each layer. However, larger scale and more complex structures affect radiative transport in other organs. Methods to create more complex phantoms have been developed to simulate the optical environment of subcutaneous blood vessels[18,19] and even whole organs, such as the bladder[20]. Modeling light transport in the lungs provides a unique problem

due to the branching structure of the air-tissue interface; a solid phantom would not likely replicate radiative transport in the organ accurately[21]. To describe a method for incorporating complex structure into an optical phantom, we describe a method to create an internal, reproducible fractal tree void that represents the three-dimensional (3D) macroscopic structure of the airway (**Figure 1**).

In the past few decades, 3D printing has become a predominant method for rapid prototyping of medical devices and models[22], and optical tissue phantoms are no exception. 3D printing has been used as an additive manufacturing tool for fabricating optical phantoms with channels[23], blood vessel networks[24], and whole-body small animal models[25]. These methods use one or two printing materials with unique optical properties. Methods have also been developed to tune the optical properties of the printing material to mimic general, turbid biological tissue[25,26]. However, the range of achievable optical properties are limited by the printing material, usually a polymer such as acrylonitrile butadiene styrene (ABS)[26], so this method is not suitable for all biological tissues. Polydimethylsiloxane (PDMS) is an optically clear polymer that can be readily mixed with scattering and absorbing particles with a higher level of tunability[27,28]. PDMS has also been used to mold phantoms with aneurysm models for deployment of embolic devices[29,30]. These phantoms also utilize a dissolvable 3D printed part, but remain optically clear for visualizing device deployment. Here, we combine this method with tunability of the optical properties of PDMS with scattering and absorbing particles to fabricate a preliminary model of the tissue and airways of the murine lung.

While the phantom presented here is specific to the lungs, the process can be applied to a variety of other organs. 3D printing of the internal structure of the phantom allows the design to be customizable for any purpose and printable scale, whether it be a blood or lymph vessel network, bone marrow, or even the four chambered structure of the heart[31]. Because we are interested in optical imaging and modeling of the lung[32,33,34], we have opted to use a four-generation fractal tree as the internal structure to replicate within the polymer phantom. This structure was designed to approximate the branching structure of the airway and have break-away support material for the 3D printing process. A more anatomically correct airway could be printed if break-away support material is not necessary. Although this particular model represents an airway, the internal structure of the phantom does not have to remain a material void. Once the surrounding polymer is cured and the 3D printed part is dissolved, the internal structure can be used as a flow pathway or as a secondary mold for a material with its own unique absorption and scattering characteristics. For example, if the internal structure from this protocol was designed as a digital bone rather than an airway, the bone structure could be 3D printed, molded with PDMS with optical properties of the finger, and then dissolved out of the phantom. The void could then be filled with a PDMS mixture with different optical properties. Additionally, each mold is not limited to a single dissolvable part. A phantom of the finger could be created to include bone, veins, arteries, and a general soft tissue layer, each with its own unique optical properties.

Protocol

1. Selection and Verification of Matrix Material Properties

1. Before starting the phantom fabrication process (**Figure 1**), find the absorption and reduced scattering coefficients for the biological tissue of interest at the imaging wavelength(s). Preliminary estimates may be found in the references[35,36]. However, validation of the optical coefficients might be necessary.
2. Using the look-up tables for absorption coefficient, μ_a, and reduced scattering coefficient, μ_s', at 488, 535, 632, and 775 nm wavelengths (**Tables 1–4** and **Figures 2–3**), select the concentrations of India ink and titanium dioxide (TiO_2) that approximate the desired optical properties. These recipes are specific to phantoms fabricated with PDMS. As these tables provide experimental data at discrete wavelengths, optimization of the recipe may be required for the specific application.
3. **Fabricate a polydimethylsiloxane (PDMS) slab of the selected recipe for confirmation of optical properties.**
    1. Using a 10:1 ratio in weight of PDMS resin to curing agent, pour ingredients into the mixing cup in the following order: PDMS resin, TiO_2, India ink, PDMS curing agent.
    NOTE: Here, we test two recipes: 1) 2 mg TiO_2 + 3.5 µL India ink per g PDMS and 2) 1 mg TiO_2 + 10 µL India ink per g PDMS. For each recipe, 4.5 g PDMS resin and 0.45 g PDMS curing agent are used with the corresponding amounts of optical particles.
    2. Mix in a speed mixer (see **Table of Materials**) for 60 s. If TiO_2 particles stick to the mixing cup (probable with high concentrations of TiO_2), mix by hand to remove the particles from the base of the cup, and mix in the mixer for another 30 s.
    3. Pour the mixture into wells or Petri dishes to make thin (0.1-1 mm) slabs of the mixture.
    4. Degas the slabs for 10 min by placing them in an air-tight negative pressure chamber, then place in a pre-heated oven at 80 °C for 30-60 min. Remove from oven and let cool.
    5. Remove the cooled polymer slab from its container. Trim off the edges to leave a flat, uniform slab. Measure the thickness of the slab using calipers.

4. **Measure transmittance (T) and reflectance (R) of slab(s) using an integrating sphere. Additional details and instructions can be found in the Inverse-Adding Doubling (IAD) manual[37].**
    1. Turn on the light source and spectrometer of the integrating sphere setup. Check the alignment of the system to ensure a small, collimated beam is centered on the entry and exit ports of the integrating sphere.
    2. Calibrate the integrating sphere system.
        1. Turn off the source, cap the exit port of the integrating sphere, and record three dark spectra.
        2. Turn the source back on to obtain the transmission reference with the exit port capped and the entrance port empty. Record three spectra.
        3. Obtain reflectance reference measurements using reflectance standard(s). Place each standard at the exit port of the sphere. Record three spectra for each reflectance standard.
    3. Measure the transmittance of the slab. With the cap on the exit port, place the slab on the entry port of the integrating sphere for the transmission measurement. Record three spectra.
    4. Measure the reflectance of the slab. Remove the exit port cap and place the slab on the exit port for the reflectance measurement. Record three spectra.

5. **Determine optical properties using IAD software. A full tutorial on the software can be found in the IAD manual with the software download[37,38].**
    1. Average the three spectra acquired for each measurement.
    2. Using the equations in the IAD manual[37], convert these measurements to R and T values. If necessary, condense the files by reducing the sampling rate along the spectrum.
    3. Prepare the input .rxt file (**Supplemental Material 1**) for IAD with the wavelengths, reflectance, transmittance, and sample thickness as described in the IAD manual[37]. Using the command prompt (Windows OS) or terminal (Mac OS), navigate to the correct path. Type "iad 'input file name'" to run IAD. The software will produce an output text file with the estimated optical properties.

6. If the optical properties are not within an acceptable range (~15%) of the desired values, modify the recipe accordingly and repeat steps 1.3–1.5.

2. Preparation of Dissolvable 3D Printed Internal Structure

1. Design internal structure using computer aided design (CAD) software. Convert structure solid model to a stereolithography file for fabrication on a 3D printer. If available, a segmented CT scan can also be converted into a stereolithography file rather than drawing a solid model of the internal structure.
   NOTE: The CAD file for the fractal tree structure used here is provided in **Supplemental Material 2**. The printer used in this paper is an extruding printer, so the part was designed to have break-away support material.
2. Select a dissolvable material for printing, such as poly-vinyl alcohol (PVA) or high-impact polystyrene (HIPS) (see **Table of Materials**). Print the solid model in this dissolvable material.
3. When printed parts are sufficiently cooled, break, dissolve, or machine the support material off of the printed part. File or sand off any large imperfections.
4. **Vapor polish the printed part to reduce surface roughness.**
    1. With the printed part secured in a vice, drill a through hole with clearance for a thin steel or nitinol wire in the base of the printed part.
    2. Thread a stainless steel or nitinol wire through the hole. Bend ends of wire and hook together. This will allow for the part to be fully immersed in acetone vapor within the beaker. Set wire and part aside.
    3. Fill a large beaker roughly 10% full of acetone. Place beaker on a hot plate while heating to 100 °C. CAUTION: Perform this step in a fume hood to prevent inhalation of acetone vapor.
    4. When acetone vapor condensation reaches about halfway up the wall of the beaker, hang the looped wire with the mock airway on a second wire and suspend in acetone vapor for 15–30 s. Ensure printed parts do not touch the beaker walls or each other (if vapor polishing multiple parts at once).
    5. Remove printed part and suspend over empty beaker or container. Let part dry for at least 4 h.

5. Verify the dimensions of the internal structure are within tolerance to the CAD design, as needed. Depending on accuracy requirements, calipers or a 3D laser scanner can be used to measure the structure.

3. Construction of Heat Resistant Mold

NOTE: Prepare a leak-proof, heat-resistant mold to form the PDMS phantom. Select a mold geometry to best fit the final phantom design. Here, a reusable rectangular mold is described.

1. Design a solid model base of the mold to 3D print. This mold is designed for a phantom with a base of 1.17 cm x 1.79 cm. The base of the mold has a 1 mm thick and 5 mm deep recess with inner dimensions matching the base of the phantom. This allows the mold to sidings to be removed and the mold to be disassembled and re-used.
2. Print a base for the mold with an inset of sufficient width to secure the sidings of the mold.
3. Place sidings in the recesses of the mold base. Here, 1 mm thick polycarbonate sheets are used as mold sidings.
4. Using heat resistant tape, seal the edges of the mold. It is imperative that all corners and edges are sufficiently sealed with no bubbles in the tape to prevent any leakage during the molding process.
5. Place a polycarbonate base plate inside the mold prepared in step 3.4. This base plate is the same 1 mm thick polycarbonate sheet as the mold siding and gives the phantom base a smooth surface without the roughness of the 3D printed surface of the mold base. Glue the fully-dried vapor polished part to the base plate. Allow sufficient time for glue to dry.

4. Fabrication of Polymer Phantom

NOTE: Use the verified recipe for the bulk matrix material determined in step 1 for the specific application. The protocol here provides the steps for a healthy murine lung tissue phantom at 535 nm with μ_s' of 40 cm^{-1} and μ_a of 2 cm^{-1}. It may be useful to fabricate a second phantom with no optical particles to use as a reference in the fabrication process.

1. Pour 9.1 g of PDMS resin into a plastic mixing cup. Add 20 mg of rutile TiO_2, followed by 35 µl of India ink. Finally add 0.91 g of curing agent to the top of the mixture. Follow the mixing protocol in step 1.3.2.
2. Pour final polymer mixture into the heat-resistant mold.
3. Pour a small amount of the mixture into a separate container to create a polymer slab for confirmation of material optical properties. Ensure enough polymer is poured to have a slab of at least 100 µm thickness.
4. Place both the mock airway mold and the separate slab into a bell jar for degassing. Begin vacuum process. If the polymer in the mock airway mold starts to rise, let the air back into the bell jar to burst the surface bubbles, then begin to pull air again. Repeat this process until the polymer does not rise significantly. This will take between 5-10 min depending on how much air was trapped during step 4.2. Once the PDMS no longer rises, continue to degas for another 15 min.

5. After degassing, slowly let the air back into the chamber. Remove both the mock airway phantom and the polymer slab and place in level oven at 80 °C for 2 h.
6. Remove the phantom and slab from the oven and let cool for 20 min. Disassemble the polymer mold with a scalpel without cutting the cured polymer. Snap the base plate off of the mock-airway base.
7. Place phantom in a heated (60 °C) ~0.5 M sodium hydroxide (NaOH) base bath until the internal part is fully dissolved. An optically clear reference phantom may help to determine the dissolving time for the internal component. Once internal structure is dissolved, take phantom out of the bath and let fully dry (~24 h) before taking any optical measurements.

5. Verification of Phantom Fabrication

1. Verify phantom geometry using high resolution magnetic resonance imaging (MRI) or micro-computed tomography (CT) imaging, if desired. These methods provide a 3D verification of internal structures within turbid material with axial resolutions of <400 μm[39,40]. Alternatively, an optically clear reference phantom can be optically imaged for verification that the printed part is fully dissolved and the remaining void is the correct geometry.
   NOTE: We have verified the internal geometry of an optically opaque phantom (2 mg TiO_2 + 3.5 μl India ink) with micro-CT on a North Star Imaging (NSI) X50. The phantom was imaged with 20 μm resolution in all dimensions (**Supplemental Materials 3, 4**).
2. Verify optical properties of the phantom using the polymer slab and the integrating sphere (described in steps 1.5–1.6).

Representative Results

To demonstrate the phantom fabrication technique, mouse lung tissue phantoms were fabricated to simulate measured optical properties of excised healthy and inflamed murine lung tissue at 535 nm (**Table 5**). This wavelength of interest is the excitation wavelength for tdTomato fluorescent protein used in recombinant reporter strains of mycobacteria in previous studies[33]. Optical measurements of mouse lung tissue were obtained with the same methods described in steps 1.4–1.5. Use of animals was approved by the Institutional Animal Care and Use Committee (IACUC) at Texas A&M University. A suitable ratio of TiO_2 to India ink was found for both healthy and inflamed murine lung tissue for 535 nm wavelength light (**Table 5**).

Recipes for materials with different optical properties are shown in **Tables 1-4** and graphically in **Figures 2**–**3**. The dependence of absorption and scattering on particle concentration are summarized in **Figure 4**. Trends in absorption coefficient and reduced scattering coefficient for phantoms with a constant concentration of TiO_2 (scattering particle) (**Figure 4A**, **4B**) and a constant concentration of India ink (absorbing particle) (**Figure 4C, 4D**) demonstrate the relation of optical properties to both particles. To ensure reproducibility of these optical properties, proper mixing technique must be used. Settling and ribboning of TiO_2 particles will cause a shift in the scattering coefficient of the cured phantom (**Figure 5**). India ink staining the mixing container will also reduce the absorption coefficient.

The lung phantoms were designed using a fractal tree structure for the internal void (**Figure 1C**). The 3D printed structure must be vapor polished to create a smooth internal surface inside the phantom (**Figure 1E**). **Figure 6** shows a comparison of light scattering from a phantom that was not degassed or vapor polished (**Figure 6A, C**), and a phantom that had a vapor polished internal part and was degassed (**Figure 6B, 6D**). The phantoms were imaged using illumination from an external white light source (**Figure 6A, 6B**) and with an internal microendoscope source at 535 nm (**Figure 6C, 6D**). Vapor polishing and degassing minimize the presence of irreproducible scatterers, including surface roughness (**Figure 6C**, inset 2) and bubbles (**Figure 6C**, inset 1). Degassing is particularly important, because air bubble location is random and unpredictable. Furthermore, air bubbles are obscured once TiO_2 particles are incorporated (not shown in **Figure 6**), making the phantom optically opaque. Therefore, unseen bubbles may undermine the phantom material's representation of tissue optical properties.

The vapor-polished 3D printed part was measured with calipers at the base and at the distal branches, and dimensions are compared to the 3D solid model in **Table 6**. Following fabrication of the polymer phantom, the phantom was imaged using a micro-CT imaging system (**Supplemental Material 3**). Using the 3D dataset, dimensions of the internal void at the base and distal branches were measured for comparison (**Table 6**). The vapor polished tree is slightly smaller at the base because the smoothing of the surface by the acetone vapor causes the surface of the plastic to flow. With the 3D printed part suspended by the base, the surface flows towards the distal branches, causing a small change in dimension of the part. There is a trade-off between surface smoothness and maintaining part size. A longer vapor polish will result in a smoother surface, but will cause more material to flow, resulting in altered dimensions.

Phantoms were imaged in an *in vivo* imaging system with an access port for insertion of a microendoscope fiber bundle (**Figure 7**). The microendoscope was placed into the void within the phantoms from which the printed part had been dissolved. The microendoscope was used for internal illumination at 535 nm and the IVIS illumination pathway was blocked. The placement of the microendoscope is indicated in **Figure 7A**. The IVIS was used for external collection of signal. Phantoms imaged had the same internal structure as those imaged in **Figure 3**. With identical internal structures and external dimensions, the difference in optical properties between healthy lung tissue (**Figure 7A**) and infected lung tissue (**Figure 7B**) is apparent in the surface irradiance of the phantoms. As these phantoms maintain an appropriate response to a change in optical properties, this method for phantom fabrication can be applied for phantoms used in internal illumination studies.

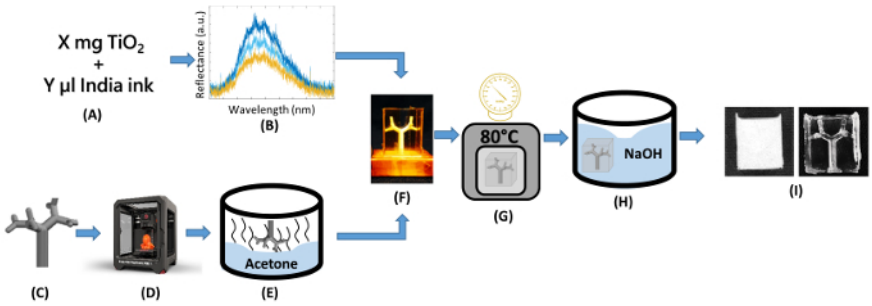

Figure 1: Flow diagram of fabrication of optical tissue phantom. (A) Determine optimal recipe for target optical properties of tissue of interest. **(B)** Verify recipe. **(C)** Design internal structure. **(D)** Print internal structure using dissolvable material. **(E)** Vapor polish printed part to smooth surface. **(F)** Mix polymer and optical particles, and pour into heat-resistant mold. **(G)** Degas and cure polydimethylsiloxane (PDMS). **(H)** Dissolve printed part to create internal void. **(I)** Verify phantom geometry and optical properties. Please click here to view a larger version of this figure.

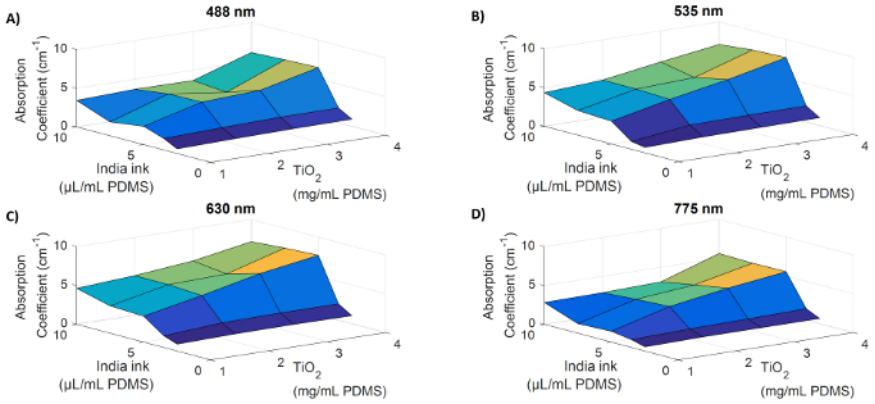

Figure 2: Trends in absorption coefficient for India ink and TiO_2 concentration. Absorption coefficients are shown for a range of India ink and titanium dioxide concentrations at 488 nm **(A)**, 535 nm **(B)**, 630 nm **(C)**, and 775 nm **(D)**. Absorption is low for low concentrations for both particles, and generally increases with concentrations of each particles. A plateau is reached between 5–7.5 µL India ink per mL PDMS. The rate of increase depends on the concentration of the other particle and the wavelength. Please click here to view a larger version of this figure.

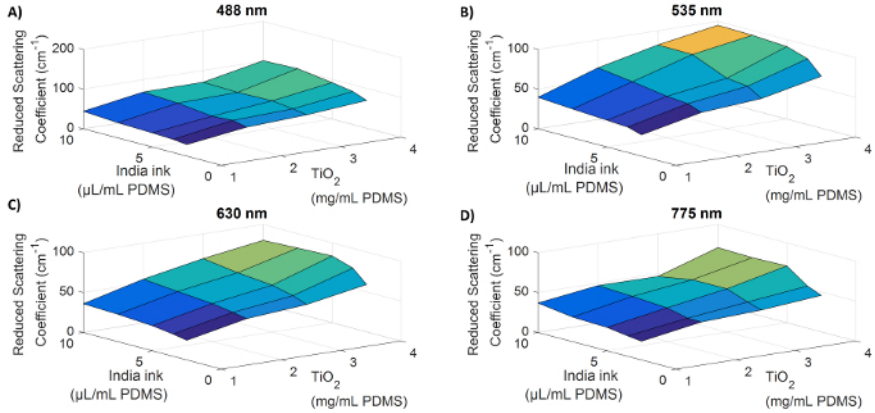

Figure 3: Trends in reduced scattering coefficient for India ink and TiO_2 concentration. Reduced scattering coefficients are shown for a range of India ink and titanium dioxide concentrations at 488 nm **(A)**, 535 nm **(B)**, 630 nm **(C)**, and 775 nm **(D)**. The reduced scattering coefficient is low for low concentrations for both particles, and generally increases with concentrations of each. Like absorption, the rate of increase depends on the concentration of the other particle and the wavelength. Please click here to view a larger version of this figure.

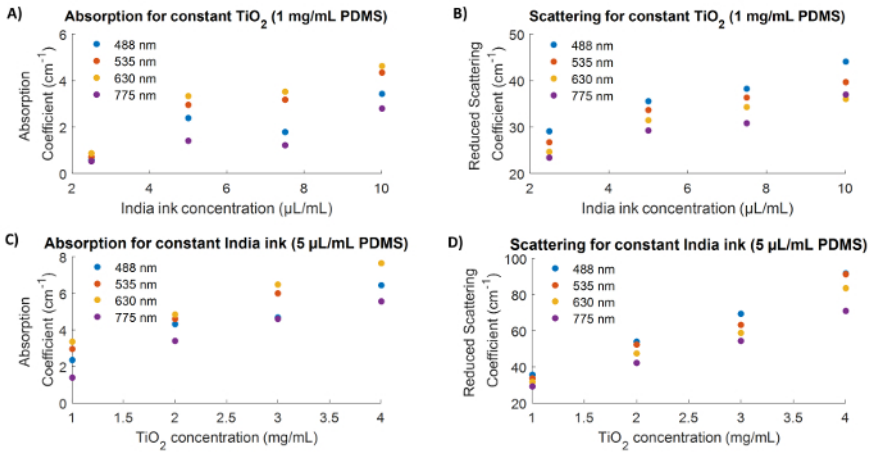

Figure 4: Interdependency of optical properties on India ink and TiO_2 concentration. Absorption coefficients and reduced scattering coefficients are shown for recipes with a constant TiO_2 concentration of 1 mg/mL PDMS **(A, B)** and constant India ink concentration of 5 µL/mL PDMS **(C,D)**. Panel **(B)** shows that scattering coefficient will change with a constant TiO_2 concentration when India ink concentration is varied, and panel **(C)** shows that absorption coefficient will change for a constant India ink concentration when TiO_2 is varied. Please click here to view a larger version of this figure.

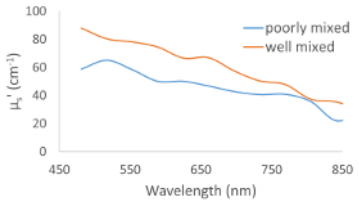

Figure 5: **Mixing effects on optical scattering.** Improper mixing of the uncured polymer and optical particles can result in a shift in the optical properties. The poorly mixed phantom represented in this figure showed settling of TiO_2 particles prior to curing. Please click here to view a larger version of this figure.

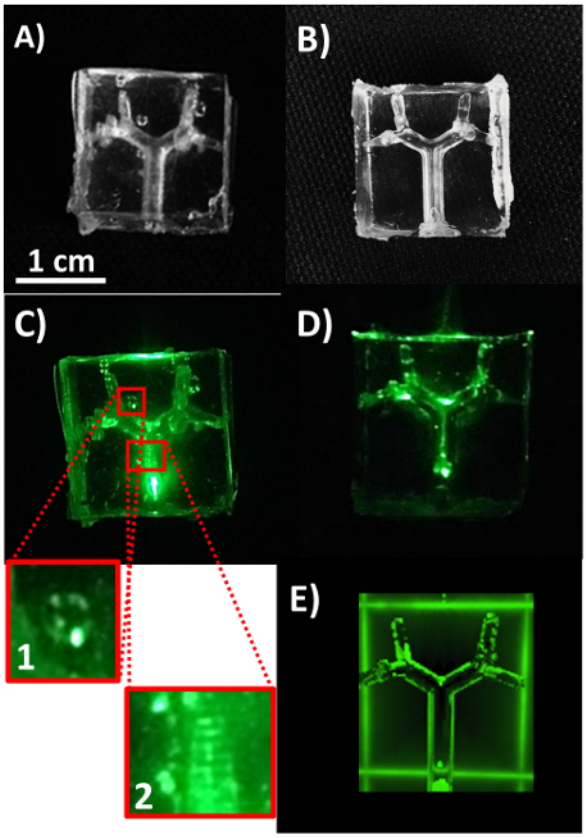

Figure 6: Representative airway phantoms with low scattering coefficient material to illustrate successful and suboptimal fabrication. Vapor polishing and degassing are integral steps in producing a phantom that has minimal uncharacterized scattering elements. **(A-B)** White light images of phantoms without vapor polishing and degassing **(A)** and with vapor polishing and degassing **(B). (C-D)** Phantoms from A-B are illuminated with 535 nm light. Insets from **(C)** are shown to depict scattering effects of 1) air bubbles and 2) a rough 3D printed surface. **(E)** Rendering of an optical simulation based on the computer aided design (CAD) model used for the phantom fabrication. Please click here to view a larger version of this figure.

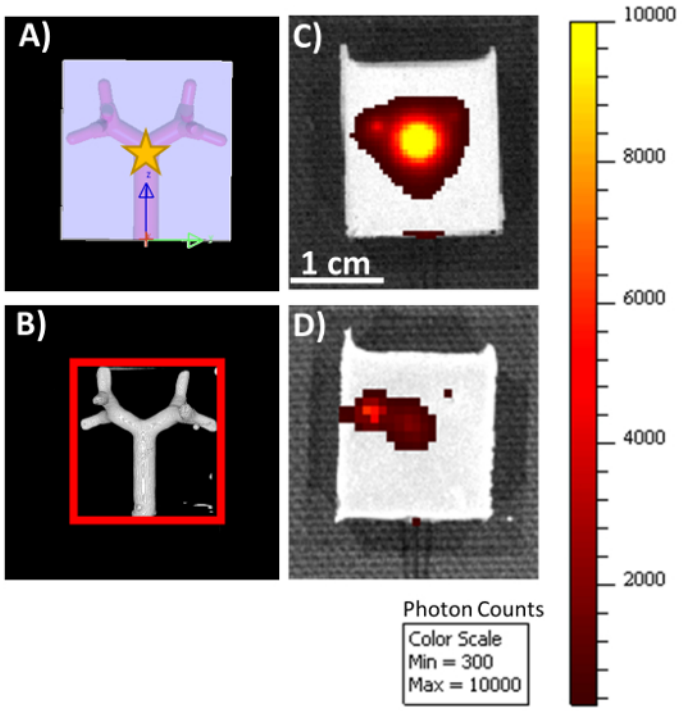

Figure 7: Imaging of phantoms with internal illumination. A computer simulation of the phantom **(A)** demonstrates the orientation of the internal geometry and source placement (yellow star) for the phantom images in panels **(C)** and **(D)**. A segmented micro-CT scan of the healthy lung tissue phantom **(B)** confirms the internal structure is present in the optically opaque phantom. The mock airway is used as a pathway for the endoscope for internal illumination of the optical phantoms at a wavelength of 535 nm. The two phantoms imaged with internal illumination are identical in external shape and internal structure, with material optical properties optimized for healthy **(C)** and inflamed **(D)** lung tissue. All images and renderings are on the same scale. Scale bar = 1 cm (panel C). Please click here to view a larger version of this figure.

488 nm	μ_s (cm^{-1})									
μ_s' (cm^{-1})	0.5	1	1.5	2	2.5	3	3.5	4	4.5	6.5
30	1 mg TiO_2 + 2.5 uL India ink	---	---	---	---	---	---	---	---	---
40	---	---	---	1 mg TiO_2 + 7.5 uL India ink	1 mg TiO_2 + 5 uL India ink	---	1 mg TiO_2 + 10 uL India ink	---	---	---
50		2 mg TiO_2 + 2.5 uL India ink	---	---	---	---	---	2 mg TiO_2 + 5 uL India ink	---	---
60	---	---	2 mg TiO_2 + 3.5 uL India ink	---	---	3 mg TiO_2 + 7.5 uL India ink	---	---	3 mg TiO_2 + 5 uL India ink	---
70	---	4 mg TiO_2 + 2.5 uL India ink	---	---	---	---	---	---	---	---
80	---	---	---	4 mg TiO_2 + 3.5 uL India ink	---	---	---	---	---	---
90	---	---	---	---	---	---	---	---	---	4 mg TiO_2 + 5 uL India ink

Table 1: Look-up table for 488 nm.

535 nm	μ_a (cm^{-1})						
μ_s' (cm^{-1})	0.5	1	2	3	4.5	6	7
30	1 mg TiO_2 + 2.5 uL India ink	---	---	1 mg TiO_2 + 5 uL India ink	---	---	---
40	---	2 mg TiO_2 + 2.5 uL India ink	---	1 mg TiO_2 + 7.5 uL India ink	1 mg TiO_2 + 10 uL India ink	---	---
50	---	---	2 mg TiO_2 + 3.5 uL India ink	---	2 mg TiO_2 + 5 uL India ink	---	---
70	---	4 mg TiO_2 + 2.5 uL India ink	---	---	3 mg TiO_2 + 5 uL India ink	---	---
80	---	---	4 mg TiO_2 + 3.5 uL India ink	---	3 mg TiO_2 + 7.5 uL India ink	3 mg TiO_2 + 10 uL India ink	---
90	---	---	---	---	---	---	4 mg TiO_2 + 10 uL India ink

Table 2: Look-up table for 535 nm.

630 nm	μ_a (cm^{-1})							
μ_s' (cm^{-1})	1	2	3.5	4.5	5	6	6.5	7
20	1 mg TiO_2 + 2.5 uL India ink	---	---	---	---	---	---	---
30	---	---	1 mg TiO_2 + 7.5 uL India ink	---	---	---	---	---
40	2 mg TiO_2 + 2.5 uL India ink	2 mg TiO_2 + 3.5 uL India ink	---	1 mg TiO_2 + 10 uL India ink	---	---	---	---
50	---	---	---	---	2 mg TiO_2 + 5 uL India ink	---	---	---
60	4 mg TiO_2 + 2.5 uL India ink	---	---	---	3 mg TiO_2 + 7.5 uL India ink	---	3 mg TiO_2 + 5 uL India ink	---
70	---	---	---	---	---	3 mg TiO_2 + 10 uL India ink	---	---
80	---	4 mg TiO_2 + 3.5 uL India ink	---	---	---	---	---	4 mg TiO_2 + 10 uL India ink

Table 3: Look-up table for 632 nm.

775 nm		μ_a (cm^{-1})							
		0.5	1	1.5	3	3.5	4.5	5.5	6
μ_s' (cm^{-1})	20	1 mg TiO_2 + 2.5 uL India ink	---	---	---	---	---	---	---
	30	---	1 mg TiO_2 + 7.5 uL India ink	1 mg TiO_2 + 5 uL India ink	---	---	---	---	---
	40	2 mg TiO_2 + 2.5 uL India ink	2 mg TiO_2 + 3.5 uL India ink	---	1 mg TiO_2 + 10 uL India ink	2 mg TiO_2 + 5 uL India ink	---	---	---
	50	4 mg TiO_2 + 2.5 uL India ink	---	4 mg TiO_2 + 3.5 uL India ink	3 mg TiO_2 + 10 uL India ink	3 mg TiO_2 + 7.5 uL India ink	3 mg TiO_2 + 5 uL India ink	---	---
	70	---	---	---	---	---	---	4 mg TiO_2 + 5 uL India ink	4 mg TiO_2 + 10 uL India ink

Table 4: Look-up table for 775 nm.

	Absorption Coefficient (cm^{-1})	Reduced Scattering Coefficient (cm^{-1})
Healthy mouse lung tissue	2.05 ± 0.58	52.69 ± 7.83
Healthy phantom (2 mg TiO_2 + 3.5 µL India ink)	1.96 ± 0.699	49.66 ± .12
Inflamed mouse lung tissue	5.49 ± 1.32	38.94 ± 9.68
Inflamed phantom (1 mg TiO_2 + 10 µL India ink)	4.34 ± 0.873	39.56 ± 5.02

Table 5: Measured optical properties of phantom recipes correspond to the measured optical properties of healthy and inflamed mouse lung tissue at 535 nm.

	Base diameter (mm)	Distal branch diameter (mm)
Solid model	2.7	1.38
Vapor polished print	2.56 ± 0.026	1.38 ± 0.141
PDMS mold (measured from CT)	2.55 ± 0.021	1.39± 0.055

Table 6: Verification of the internal structure of the phantom.

Supplemental Material 1: Example IAD input file. Please click here to download this file.

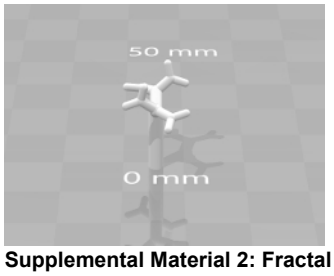

Supplemental Material 2: Fractal tree airway solid model. Please click here to download this file.

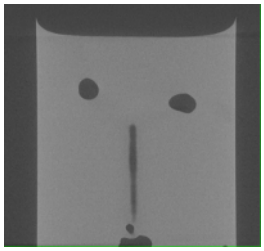

Supplemental Material 3: Micro-CT fly-thru of phantom modeling healthy mouse lung tissue. Please click here to download this file.

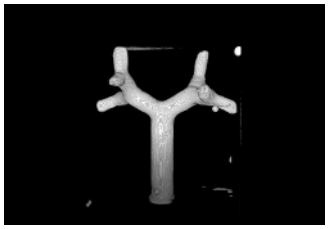

Supplemental Material 4: Video of rotating segmented micro-CT scan. Please click here to download this file.

Discussion

We have demonstrated a method for creating optical phantoms to represent a murine lung with an internal branching structure to simulate the internal air-tissue interface. The optical properties of murine lung tissue are achieved by incorporating unique concentrations of optically scattering and absorbing particles distributed homogenously within the bulk matrix polymer. These optical properties can be tuned to mimic the physiological values within different spectral ranges of tissues in different states (*i.e.* healthy versus diseased tissue). The optical properties are dependent on the wavelength of interest, the base material, and the concentrations of the particles within the phantom. However, with multiple particles, the relationship between scattering and absorption is not always intuitive[41]. The rate of increase of absorption is dependent on the concentration of the scattering particle as well as the absorbing particle, and likewise for the rate of increase of the reduced scattering coefficient. (**Figures 2-4**). PDMS phantoms have also been shown to maintain their optical properties for up to 1 year[27,28]. We have measured a 3-week stability of optical properties within the error of our integrating sphere measurements (<15%). Storage of these phantoms and standards in a light-tight container can help preserve their optical properties for longer periods of time.

Vapor polishing the dissolvable printed part allows for a reproducible smooth surface on the internal air interface of the phantom (**Figure 6**). For the fractal geometry shown here, polishing the internal structure yielded a decrease in average surface roughness of molded PDMS from 37.4 µm to 7.2 µm. This is extremely important if the phantom is used for validation of an optical simulation because a rough surface is much more difficult to accurately simulate than a smooth, uniform surface (**Figure 6E**). Degassing is also very important due to the fact that bubbles within the PDMS phantom act as optical scatterers (**Figure 6C**, inset 1). Bubble location is not predictable to replicate in a simulation, and could skew results if the phantom is used as a calibration standard.

After verification with micro-CT, a small amount of residual material was found within the airway void (**Supplemental Material 3**). Additionally, a segmentation of this same CT scan reveals a small air bubble next to the branching structure (**Supplemental Material 4**). During fabrication, optically clear phantoms yielded a full dissolution of the material of the internal structure and no air bubbles within the polymer matrix. Verification with micro-CT showed that the optically opaque phantoms may contain small flaws, not otherwise visible.

Properly mixing the optical particles with the uncured polymer is imperative to achieve reproducible and predictable optical absorption and scattering. A shift in the reduced scattering coefficient caused by poor mixing is shown in **Figure 5**. Before pouring the polymer into the mold, ensure there is no evidence of TiO_2 particles settling or "ribboning" in the mixture and no evidence of India ink staining the mixing container. Adding the particles in the recommended order should minimize these problems.

The design of these phantoms is limited by the 3D printed part. The mock airway is designed so that the support material can be pried off, as it is not dissolvable. This can be overcome by moving to a more advanced printer that can either print materials with varying solubility, or a laser sintering printer, that does not need support material. It is also important to note that the lung is inherently a very porous organ because of the distal airways and the alveoli. While that is not represented in this phantom, the optical effects of similar structures have been observed using a Bragg-Nye bubble raft for optical coherence tomography[21], air bubbles in olive oil[42], and shaving cream or dish detergent for nuclear magnetic resonance imaging[43]. Creating polymer foams with reproducible characteristics may be able to reconcile this difference between the solid phantoms presented here and the lung microstructure[44].

The shape of the final phantom can also be customized depending on the application. The rectangular phantom shown here was imaged with internal illumination and used for validation of a computational model of healthy and infected lungs (**Figure 7**). This design can be updated further to represent the cylindrical torso of the mouse by simply changing the design of the external polymer mold.

While we have detailed here the design of a murine lung and airway phantom, these methods can be modified to fit other organs or animals of interest. The internal structure can be converted to a flow pathway for vascular phantoms, or can be used as a cast for a complex internal structure with unique optical properties. The overall shape of the phantom can also be tuned to the application, animal, or organ of interest. 3D printing of both internal structures and polymer molds gives freedom to the design process of structured polymer optical phantoms. These are

integral tools in simulation validation and calibration of *in vivo* optical imaging techniques, because they can more accurately represent the *in vivo* environment than homogeneous single or multi-layer phantoms.

Disclosures

The authors have nothing to disclose.

Acknowledgements

This work was supported by the National Science Foundation CAREER award no. CBET-1254767 and National Institute of Allergy and Infectious Diseases grant no. R01 AI104960. We gratefully acknowledge Patrick Griffin and Dan Tran for their assistance with characterization measurements and the Texas A&M Cardiovascular Pathology Laboratory for micro-CT imaging.

References

1. Curatolo, A., Kennedy, B. F., Sampson, D. D. Structured three-dimensional optical phantom for optical coherence tomography. *Opt Express.* **19** (20), 19480-19485 (2011).
2. Miranda, D. A., Cristiano, K. L., Gutiérrez, J. C. Breast phantom for mammary tissue characterization by near infrared spectroscopy. *J Phys Conf Ser.* **466** (1), 012018 (2013).
3. Solomon, M. *et al.* Multimodal Fluorescence-Mediated Tomography and SPECT/CT for Small-Animal Imaging. *J Nucl Med.* **54** (4), 639-646 (2013).
4. Wagnières, G. *et al.* An optical phantom with tissue-like properties in the visible for use in PDT and fluorescence spectroscopy. *Phys Med Biol.* **42** (7), 1415-1426 (1997).
5. Rajaram, N., Reesor, A. F., Mulvey, C. S., Frees, A. E., Ramanujam, N. Non-Invasive, Simultaneous Quantification of Vascular Oxygenation and Glucose Uptake in Tissue. *PLoS ONE.* **10** (1), e0117132 (2015).
6. Niedre, M. J., Turner, G. M., Ntziachristos, V. Time-resolved imaging of optical coefficients through murine chest cavities. *J Biomed Opt.* **11** (6), 064017 (2006).
7. Schmidt, F. E. W. *et al.* Multiple-slice imaging of a tissue-equivalent phantom by use of time-resolvedoptical tomography. *Appl Opt.* **39** (19), 3380-3387 (2000).
8. Cerussi, A. E. *et al.* Tissue phantoms in multicenter clinical trials for diffuse optical technologies. *Biomed Opt Express.* **3** (5), 966-971 (2012).
9. Marín, N. M. *et al.* Calibration standards for multicenter clinical trials of fluorescence spectroscopy for in vivo diagnosis. *J Biomed Opt.* **11** (1), 014010 (2006).
10. Alexandrakis, G., Rannou, F. R., Chatziioannou, A. F. Tomographic bioluminescence imaging by use of a combined optical-PET (OPET) system: a computer simulation feasibility study. *Phys Med Biol.* **50** (17), 4225-4241 (2005).
11. Wan, Q., Beier, H. T., Ibey, B. L., Good, T., Coté, G. L. in *Optical Diagnostics and Sensing VII.* eds Gerard L. Coté & Alexander V. Priezzhev) 64450J (SPIE) (2007).
12. Chen, C. *et al.* Preparation of a skin equivalent phantom with interior micron-scale vessel structures for optical imaging experiments. *Biomed Opt Express.* **5** (9), 3140-3149 (2014).
13. Pogue, B. W., Patterson, M. S. Review of tissue simulating phantoms for optical spectroscopy, imaging and dosimetry. *J Biomed Opt.* **11** (4), 041102 (2006).
14. Wróbel, M. S. *et al.* Use of optical skin phantoms for preclinical evaluation of laser efficiency for skin lesion therapy. *J Biomed Opt.* **20** (8), 085003 (2015).
15. Cubeddu, R., Pifferi, A., Taroni, P., Torricelli, A., Valentini, G. A solid tissue phantom for photon migration studies. *Phys Med Biol.* **42** (10), 1971-1979 (1997).
16. Bae, Y., Son, T., Park, J., Jung, B. Fabrication of a thin-layer solid optical tissue phantom by a spin-coating method: pilot study. *J Biomed Opt.* **18** (2), 025006 (2013).
17. Park, J. *et al.* in *Design and Performance Validation of Phantoms Used in Conjunction with Optical Measurement of Tissue V.* (ed Robert J. Nordstrom) 85830G (SPIE) (2013).
18. Luu, L., Roman, P. A., Mathews, S. A., Ramella-Roman, J. C. Microfluidics based phantoms of superficial vascular network. *Biomed Opt Express.* **3** (6), 1350-1364 (2012).
19. Chen, A. I. *et al.* Multilayered tissue mimicking skin and vessel phantoms with tunable mechanical, optical, and acoustic properties. *Med Phys.* **43** (6Part1), 3117-3131 (2016).
20. Lurie, K. L., Smith, G. T., Khan, S. A., Liao, J. C., Ellerbee, A. K. Three-dimensional, distendable bladder phantom for optical coherence tomography and white light cystoscopy. *J Biomed Opt.* **19** (3), 036009 (2014).
21. Golabchi, A. *et al.* Refractive errors and corrections for OCT images in an inflated lung phantom. *Biomed Opt Express.* **3** (5), 1101-1109 (2012).
22. Rengier, F. *et al.* 3D printing based on imaging data: review of medical applications. *Int J Comput Assist Radiol and Surg.* **5** (4), 335-341 (2010).
23. Wang, J. *et al.* Three-dimensional printing of tissue phantoms for biophotonic imaging. *Opt Lett.* **39** (10), 3010-3013 (2014).
24. Ghassemi, P. *et al.* Evaluation of Mobile Phone Performance for Near-Infrared Fluorescence Imaging. *IEEE Trans Biomed Eng.* **64** (7), 1650-1653 (2017).
25. Bentz, B. Z., Chavan, A. V., Lin, D., Tsai, E. H. R., Webb, K. J. Fabrication and application of heterogeneous printed mouse phantoms for whole animal optical imaging. *Appl Opt.* **55** (2), 280-287 (2016).
26. Diep, P. *et al.* Three-dimensional printed optical phantoms with customized absorption and scattering properties. *Biomed Opt Express.* **6** (11), 4212-4220 (2015).
27. Pogue, B. W., Patterson, M. S. Review of tissue simulating phantoms for optical spectroscopy, imaging and dosimetry. *Journal of Biomedical Optics.* **11** (4), 041102-041102-041116 (2006).

28. Bruin, D. M. *et al.* Optical phantoms of varying geometry based on thin building blocks with controlled optical properties. *J Biomed Opt.* **15** (2), 025001-025001-025010 (2010).
29. Boyle, A. J. *et al.* In vitro performance of a shape memory polymer foam-coated coil embolization device. *Med Eng Phys.* **49**, 56-62, (2017).
30. Hwang, W., Singhal, P., Miller, M. W., Maitland, D. J. In Vitro Study of Transcatheter Delivery of a Shape Memory Polymer Foam Embolic Device for Treating Cerebral Aneurysms. *J Med Dev.* **7** (2), 020932-020932-020932 (2013).
31. Giampietro Sgaragli and Maria, F. Human Tuberculosis I. Epidemiology, Diagnosis and Pathogenetic Mechanisms. *Curr Med Chem.* **23** (25), 2836-2873 (2016).
32. Mufti, N., Kong, Y., Cirillo, J. D., Maitland, K. C. Fiber optic microendoscopy for preclinical study of bacterial infection dynamics. *Biomed Opt Express.* **2** (5), 1121-1134 (2011).
33. Nooshabadi, F. *et al.* Intravital fluorescence excitation in whole-animal optical imaging. *PLoS One.* **11** (2), e0149932 (2016).
34. Nooshabadi, F. *et al.* Intravital excitation increases detection sensitivity for pulmonary tuberculosis by whole-body imaging with beta-lactamase reporter enzyme fluorescence. *J Biophotonics.* (2016).
35. Duck, F. A. *Physical Properties of Tissue: A Comprehensive Reference Book.* Academic Press, Inc., (1990).
36. Tuchin, V. V., Tuchin, V. *Tissue optics: light scattering methods and instruments for medical diagnosis.* Vol. 13 SPIE press Bellingham, (2007).
37. Prahl, S. *Everything I think you should know about Inverse Adding-Doubling.* Oregon Tech, (2011).
38. *Inverse Adding-Doubling.* v.3-9-12 (2014).
39. Link, T. M. *et al.* A Comparative Study of Trabecular Bone Properties in the Spine and Femur Using High Resolution MRI and CT. *J Bone Miner Res.* **13** (1), 122-132 (1998).
40. Batiste, D. L. *et al.* High-resolution MRI and micro-CT in an ex vivo rabbit anterior cruciate ligament transection model of osteoarthritis. *Osteoarthr cartil.* **12** (8), 614-626 (2004).
41. Greening, G. J. *et al.* Characterization of thin poly(dimethylsiloxane)-based tissue-simulating phantoms with tunable reduced scattering and absorption coefficients at visible and near-infrared wavelengths. *J Biomed Opt.* **19** (11), 115002 (2014).
42. Meissner, S., Knels, L., Krueger, A., Koch, T., Koch, E. Simultaneous three-dimensional optical coherence tomography and intravital microscopy for imaging subpleural pulmonary alveoli in isolated rabbit lungs. *J Biomed Opt.* **14** (5), 054020 (2009).
43. Morris, A. H. *et al.* A new nuclear magnetic resonance property of lung. *J Appl Phys.* **58** (3), 759-762 (1985).
44. Hearon, K. *et al.* Porous Shape Memory Polymers. *Polym Rev (Phila Pa).* **53** (1), 41-75 (2013).

